applied sciences

MDPI

Article

Multi-Layered and Homogenized Models for In-Plane Guided Wave Excitation, Sensing, and Scattering in Anisotropic Laminated Composites

Artem A. Eremin *, Mikhail V. Golub, Sergey I. Fomenko, Alexander A. Evdokimov and Polina A. Nets

Institute for Mathematics, Mechanics and Informatics, Kuban State University, 350040 Krasnodar, Russia
* Correspondence: eremin_a_87@mail.ru

Abstract: The numerical evaluation of elastic guided wave (EGW) phenomena is an important stage in the development and configuration of ultrasonic-based non-destructive testing/structural health monitoring (NDT/SHM) systems. To reduce the computational costs, which are typical for EGW simulations in laminated composite structures, and to make the corresponding parametric analysis possible, the latter could be treated by employing an effective single-layer model with homogenized anisotropic material properties. The present study investigates the applicability of such an approach to simulate EGW excitation, propagation, scattering, and sensing in laminate composite structures, which are among the typical problems for ultrasonic-based NDT/SHM. To this end, two homogenized models have been implemented: the well-known static long-wave homogenization approach and the advanced Lamb wave homogenization method, where the effect of angular and frequency dispersion of EGWs is taken into account. To illustrate their performance, in-plane elastic guided wave excitation and sensing with surface-mounted piezoelectric transducers as well as wave scattering by a T-shaped stringer in cross-ply symmetric anisotropic laminates are examined by employing a recently developed semi-analytical hybrid approach. The limits of the applicability of both homogenized models are demonstrated and discussed via the comparison with the multi-layered model. The general conclusion from the obtained results is that only a qualitative, although computationally efficient, description of the EGW phenomena in the considered composites can be achieved using single-layer models.

Keywords: guided waves; anisotropy; laminate; homogenization; piezoelectric transducer; stringer; sensing

check for updates

Citation: Eremin, A.A.; Golub, M.V.; Fomenko, S.I.; Evdokimov, A.A.; Nets, P.A. Multi-Layered and Homogenized Models for In-Plane Guided Wave Excitation, Sensing, and Scattering in Anisotropic Laminated Composites. *Appl. Sci.* **2023**, *13*, 1698. https://doi.org/10.3390/app13031698

Academic Editors: Yiming Deng and Sunil Kishore Chakrapani

Received: 30 December 2022
Revised: 24 January 2023
Accepted: 27 January 2023
Published: 29 January 2023

Copyright: © 2023 by the authors. Licensee MDPI, Basel, Switzerland. This article is an open access article distributed under the terms and conditions of the Creative Commons Attribution (CC BY) license (https://creativecommons.org/licenses/by/4.0/).

1. Introduction

Laminated composite materials are extensively used in various engineering fields such as the aerospace industry, land-vehicle manufacturing, wind and hydrogen power applications, etc. [1–4]. Among the major advantages of composite materials are their high strength-to-weight ratios and the possibility to achieve oriented mechanical properties, which can be combined to produce a laminate designed for a specific high-performance structure [1,5,6]. However, damage may still occur in such materials, which makes them an important object for emerging non-destructive testing (NDT) [7] and structural health monitoring (SHM) [8] techniques, in particular, those utilizing elastic guided waves (EGWs) as a physical basis [9,10]. Specific wave phenomena underlying EGW-based NDT/SHM techniques are including (but, of course, not limited to) EGW excitation with either contact or non-contact techniques, their propagation through or along the object, possible scattering by structural components and/or occurring damage and corresponding wave motion detection employing various sensing technologies [7–10].

Development of efficient ultrasonic wave-based diagnostic strategies adopted for composite structures requires a thorough understanding of the of elastodynamic behavior

of such materials [11–14]. Prior extensive theoretical studies allow for the optimization of NDT/SHM system performance and enhance their damage detection and characterization capabilities [15–19]. For the numerical simulation of the elastodynamic behavior of laminated composite structures, various computational techniques have been widely adopted [20], among which mesh-based methods, especially the finite element method (FEM) and its modifications, play an important role [21,22].

When a multi-layered elastic structure is discretized with the standard FEM, e.g., employing various open-source or commercially available codes [23], at least one finite element is required within the sub-layer thickness. Therefore, computational costs are growing dramatically compared to conventional metallic structures when laminated composites are simulated, especially for three-dimensional problems [23,24]. To overcome this burden, several strategies are adopted. They include the application of more sophisticated FEM algorithms, e.g., the spectral element method [25]. Relying on the specific approximation functions, it is especially beneficial for the simulation of wave propagation problems in the time domain [26]. Another alternative is to adopt approximate plate or shell theories, where the dependency of strains and displacements in the vertical direction is resolved analytically, thus reducing the model dimension by one order [27], or approximated in a more simple way than in complete 3D models [28,29]. For relatively thick composites, especially those where certain periodicity exists in stacking sequence, the whole laminate could be replaced by a single anisotropic layer [30,31]. Its effective elastic properties are obtained by employing either static [31,32] or dynamic [33] homogenization approaches. The adequacy and efficacy of such approaches considering the evaluation of EGW phenomena in various composites have been studied in Ref. [34,35]. For instance, a comparison of the static effective medium model with the exact multi-layered model for non-symmetric cross-ply laminates showed that this approximation provides similar results if the number of plies is quite large. Otherwise, it is adequate only for fundamental EGW modes at low frequencies. Such results were obtained both for phase velocity dispersion curves of fundamental and higher-order EGWs and for transient in-plane wave propagation excited by a line source.

Inspired by the recent paper [19], where the initial multi-layered composite plate in FEM simulations was replaced with a single anisotropic layer and advancing the results from papers [34,35], the current work aims at the further investigation of the applicability of equivalent single layer models for the EGW phenomena simulation related to NDT/SHM applications. For this purpose, a typical problem for ultrasonic-based NDT/SHM is considered, namely in-plane EGW excitation and sensing with surface-mounted piezoelectric wafer transducers (PWT) as well as their scattering by a T-shaped stringer in symmetric cross-ply laminates with different lamination schemes, which are examined by employing the recently developed semi-analytical hybrid approach (SAHA) [36–38]. To simulate the waveguide structure, along with the wave dynamics of a complete multi-layered structure, two homogenized models are considered. While the first one relies on a well-developed static long-wave homogenization approach [31], for the latter, dynamic homogenization is adopted based on the concept proposed in Ref. [33], which serves as a starting point. The obtained results illustrate that while homogenized models rather adequately follow the dispersion properties of the considered multi-layered structures, the output voltage of a sensing PWT either in the presence of the T-shaped stringer or in its absence could be only qualitatively represented.

2. Mathematical Models

2.1. General Problem Statement

2.1.1. Multi-Layered Waveguide

As a starting point, the three-dimensional elastic multi-layered waveguide is considered occupying the domain $\hat{V} = \{-\infty < x_1, x_2 < \infty, 0 \le x_3 \le H\}$ in the Cartesian coordinates $\boldsymbol{x} = \{x_1, x_2, x_3\}$ introduced in such a way that the plane x_1Ox_2 is parallel to the surfaces $S^- = \{x_3 = 0\}$ and $S^+ = \{x_3 = H\}$ or the outer boundaries of $\hat{V}$ ($\partial\hat{V} = S^- \cup S^+$). The waveguide $\hat{V}$ is a union of L homogeneous elastic transversally isotropic layers

$V^{(l)} = \{-\infty < x_1, x_2 < \infty, z^{(l-1)} \le x_3 \le z^{(l)}\}$ of thicknesses $h^{(l)} = |z^{(l)} - z^{(l-1)}|$ with stiffness tensor $C^{(l)}_{ijkl}$ and mass densities $\rho^{(l)}$, $l = 1, 2, ...L+1$ and $z^{(1)} = 0$, $z^{(L+1)} = H$ (see Figure 1a). Below, where it does not lead to misunderstanding, the superscript is omitted.

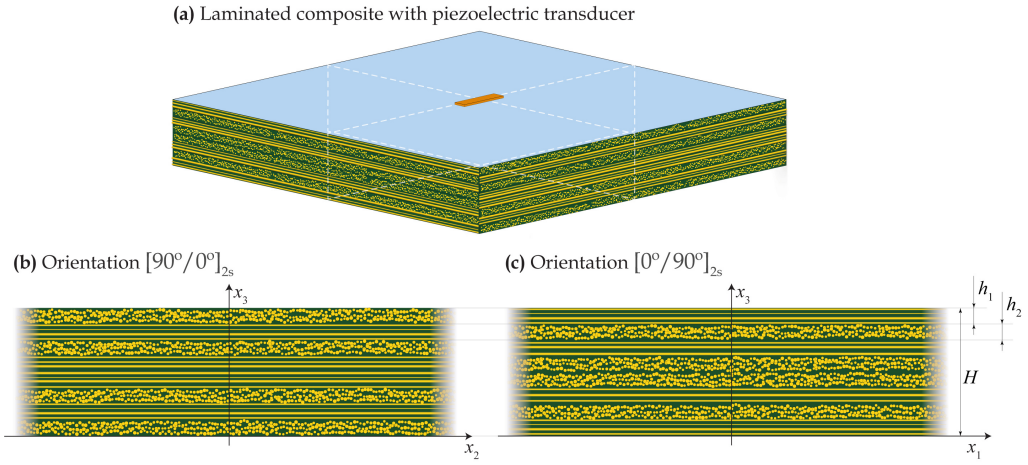


Figure 1. Multi-layered composite with a piezoelectric transducer.

Constitutive equations

$$\sigma_{ij} = C_{ijkl} s_{kl}. \tag{1}$$

relate components of stress tensor σ_{ij} and displacement vector u_i, where

$$s_{kl} = \frac{1}{2}(u_{k,l} + u_{l,k}).$$

Therefore, governing equations for time-harmonic motion $u_i e^{i\omega t}$ ($\omega = 2\pi f$ is angular frequency, and f stands for dimensional frequency) in the absence of body forces.

$$C_{ijkl} \frac{\partial^2 u_k(\boldsymbol{x})}{\partial x_l \partial x_j} + \rho\omega^2 u_i(\boldsymbol{x}) = 0 \tag{2}$$

are valid in each sub-layer $V^{(l)}$. Continuity of displacements and traction vector $\boldsymbol{\tau} = (\sigma_{13}, \sigma_{23}, \sigma_{33})$ at the interfaces between sub-layers is assumed, i.e.,

$$u_i^{(l)}\Big|_{z=z^{(l)}} = u_i^{(l+1)}\Big|_{z=z^{(l)}}, \quad \boldsymbol{\tau}_i^{(l)}\Big|_{z=z^{(l)}} = \boldsymbol{\tau}_i^{(l+1)}\Big|_{z=z^{(l)}}, \; l = 2, ..., L. \tag{3}$$

The lower boundary of the waveguide is stress free while the excitation of EGWs is achieved by applying certain traction $\boldsymbol{q}$ in a finite area Ω of its upper boundary:

$$\boldsymbol{\tau}|_{z=0} = 0, \quad \boldsymbol{\tau}|_{z=H} = \boldsymbol{q}, \tag{4}$$

and no other external loads are considered. Since an infinite waveguide is considered, to close the problem statement, the limiting absorption principle [39] is used as a radiation condition.

The geometry of the considered boundary value problem (2)–(4) allows to apply the two-dimensional Fourier transform F_{xy} over the horizontal spatial variables x_1, x_2 and to derive its explicit solution in terms of the inverse Fourier two-fold path integral [40,41]:

$$\boldsymbol{u}(\boldsymbol{x}, \omega) = \frac{1}{4\pi^2} \int_{\Gamma^+} \int_0^{2\pi} K(\alpha, \gamma, x_3) \boldsymbol{Q}(\alpha, \gamma) e^{-i\alpha r \cos(\gamma - \varphi)} d\gamma \alpha d\alpha, \tag{5}$$

where $K = F_{xy}[k]$ and $\boldsymbol{Q} = F_{xy}[\boldsymbol{q}]$ are Fourier symbols of the 3×3 Green's matrix $k(\boldsymbol{x})$ and the contact stress vector $\boldsymbol{q}(x_1, x_2)$ (the notations of Ref. [41] are employed); polar coordinates (r, φ) and (α, γ) are introduced in spatial and Fourier domains, respectively. Integration contour Γ^+ goes in the complex plane α along the real semi-axis $\mathrm{Re}\alpha \geq 0$, $\mathrm{Im}\alpha = 0$ from the real axis bypassing real poles of the Green's matrix K either from below or above according to the limiting absorption principle [39,41].

Onwards, an important case of multi-layered composite structures, namely, cross-ply laminates fabricated from identical unidirectional transversely isotropic prepregs with the general stacking sequence $[0^\circ_\eta, 90^\circ_\theta]_{p\{\mathrm{s}\}}$ are considered. Here, symbols η, θ and p denote the number of repetitions, subscript $\{\mathrm{s}\}$ might either be present or not standing for the symmetric arrangement of sub-layers and direction 0° of fiber orientation coincides with x_1 axis. Such laminates possess two natural principal axes x_1 and x_2 and support the propagation of in-plane EGWs along them [42]. Therefore, if the area Ω, to which traction $\boldsymbol{q}$ is applied, is infinitely elongated along one of these axes, the considered 3D boundary value problem could be reduced to two plane-strain problems. The latter are for waveguides with stacking sequences $[90^\circ_\eta, 0^\circ_\theta]_{p\{\mathrm{s}\}}$ (if Ω is infinite over x_1 axis) and $[0^\circ_\eta, 90^\circ_\theta]_{p\{\mathrm{s}\}}$ (if the load is applied along x_2 direction), see Figure 1b,c.

2.1.2. Homogenized Waveguide

Employing Voigt notation and assumptions regarding the transverse isotropy of unidirectional plies and their orientation (either 0 or 90 degrees), stiffness tensor C_{ijkl} could be reduced to a 6×6 stiffness matrix C_{ij} with 12 non-zero elements [42].

Taking these matrices $C^{(l)}_{ij}$, $l = 1, \ldots, L$ as a starting point, two approaches for deriving the stiffness matrix of the homogenized single layer waveguide $\bar{C}_{ij}$ are considered. Within the first model (Model 1—static long-wave homogenization (SLWH)), following relations for the components of $\bar{C}_{ij}$ are employed [31] taking into account that all the prepregs have identical thickness $h^{(l)} = H/L$:

$$\begin{gathered} \bar{C}_{ij} = \sum_{l=1}^{L} C^{(l)}_{ij}, \quad i,j = 1,2,3,6 \\ \bar{C}_{pq} = \left(\sum_{l=1}^{L} C^{(l)}_{pq} / \Delta_l \right) / \Delta, \quad p,q = 4,5, \\ \Delta_l = C^{(l)}_{44} C^{(l)}_{55}, \quad \Delta = \left(\sum_{l=1}^{L} C^{(l)}_{44} / \Delta_l \right) \left(\sum_{l=1}^{L} C^{(l)}_{55} / \Delta_l \right) \end{gathered} \tag{6}$$

From Equation (6), it is clear that if a balanced cross-ply laminate is considered, i.e., the one where $\eta = \theta$ in the stacking sequence, equalities $\bar{C}_{11} = \bar{C}_{22}$ and $\bar{C}_{44} = \bar{C}_{55}$ hold.

The second model (Model 2—Lamb wave homogenization method (LWHM)) is inspired by the approach proposed in Ref. [33]. In LWHM, the homogenization is achieved by equating at a set of given frequencies angular-dependent wavenumbers k_n of EGWs (quasi-Lamb waves), (whereas slowness surfaces of Floquet waves are employed in Ref. [33]) in an actual multi-layered composite medium to the corresponding dispersion curves of EGWs propagating in the effective anisotropic homogeneous single layer. Effective elastic constants $\bar{C}_{ij}$ in the class of orthotropic materials are obtained from the optimization of the discrepancy between these angular dispersion curves of k_n. For this purpose, an objective function is constructed from the components of the Fourier transform of the Green's matrix for the considered homogenized anisotropic waveguide [43,44]

$$F(\bar{C}_{ij}) = \sum_{r=1}^{N_f} \sum_{n=1}^{N_w} \sum_{m=1}^{N_\gamma} |K^{-1}_{33}(k_n(\gamma_m), f_r)|. \tag{7}$$

Here K_{33} is the $(3,3)$ component of the Green's matrix $K(\alpha, \gamma, f)$, of which the evaluation algorithm is taken from Ref. [41]; N_f, N_w and N_γ are the numbers of frequencies, normal modes of EGWs and propagation directions for which angular and frequency-dependent wavenumbers $k_n(\gamma_m, f_r)$ for the initial multi-layered composite are preliminarily evaluated by employing the approach described in Ref. [41]. Since poles of the Green's matrix $K(\alpha, \gamma, f)$ in the complex plane are equal to the wavenumbers k_n of normal modes propagating in the direction γ [41], appropriate values of $\bar{C}_{ij}$ would result in higher magnitudes of $|K_{33}|$. The minimization of (7) is achieved with a micro-genetic algorithm (μ-GA) [45].

To illustrate the performance and peculiarities of the implemented models, the 8-layered cross-ply laminate with the stacking sequence $[0^\circ, 90^\circ]_{2s}$ is considered with a total thickness of $H = 2.24$ mm and prepreg's density $\rho = 1528\ \mathrm{kg/m^3}$. Ply elastic properties [46] as well as the non-zero values of $\bar{C}_{ij}$ obtained with both of the described models are summarized in Table 1. For Model 2, the following parameters were considered: $N_f = 2$ ($f = 50$ and 200 kHz), $N_w = 3$, which stands for fundamental quasi-antisymmetric, symmetric, and SH-modes $A0$, $S0$ and $SH0$ respectively, and $N_\gamma = 50$ resulting in 50 γ_m points evenly distributed along the segment $\gamma \in [0, \pi/2]$. Due to the stochastic nature of μ-GA, corresponding data in Table 1 represent averaged values after 10 runs of the optimization algorithm.

Table 1. Elastic properties of a single ply and of a homogenized waveguide [GPa].

Material	C_{11}	C_{22}	C_{33}	C_{12}	C_{13}	C_{23}	C_{44}	C_{55}	C_{66}
$[0^\circ, 90^\circ]_{2s}$, ply	122.4	11.5	11.5	4.13	4.13	6.47	2.51	4.85	4.85
Model 1, SLWH	67.0	67.0	11.5	4.13	5.30	5.30	3.31	3.31	4.85
Model 2, LWHM	64.8	64.8	11.1	7.99	3.63	3.90	2.85	3.39	4.92

Angular dispersion curves for the initial multi-layered waveguide, which serve as an input for the LWHM at frequencies $f = 50$ and 200 kHz, are shown in Figure 2 together with the corresponding results obtained employing both homogenization models. Several observations could be made: while the output of the SLWH and the LWHM approaches is an orthotropic material, for the second model, $\bar{C}_{44} \neq \bar{C}_{55}$. This results in a remarkably better coincidence between $[0^\circ, 90^\circ]_{2s}$ and the LWHM for $A0$ dispersion curves, especially for higher frequencies. However, the trade-off is that for $S0$ and $SH0$ modes a slight discrepancy in $k_n(\gamma)$ near $\gamma = \pi/4$ is observed.

2.2. Guided Waves Excitation, Sensing, and Scattering

Since both of the homogenized anisotropic waveguides are orthotropic with principal axes coinciding with directions x_1 and x_2, they, as well as the initial cross-ply laminate, support propagation of in-plane EGWs along these directions. Therefore, for simplicity's sake, the problem of EGW excitation, sensing, and scattering is considered further on within the plane-strain assumption (Figure 1b,c).

In the case of two rectangular surface-mounted PWTs acting as an actuator and as a sensor, two corresponding domains ($\hat{V}^{(a)}$ and $\hat{V}^{(s)}$, upper index a stands for the actuator, while s stands for sensor) are included in the mathematical model. Two PWTs are assumed of the same length a and thickness d, being situated at the upper surface of the waveguide $\hat{S}^+$ with centers located at $s = 50$ mm from each other (see Figure 3). PWTs are assumed to be made of the same piezoelectric material with mass density $\hat{\rho}$ and the tensors of elastic, piezoelectric, and dielectric constants $\hat{C}_{ijkl}$, $\hat{e}_{kij}$, $\hat{\varepsilon}_{ik}$ respectively.

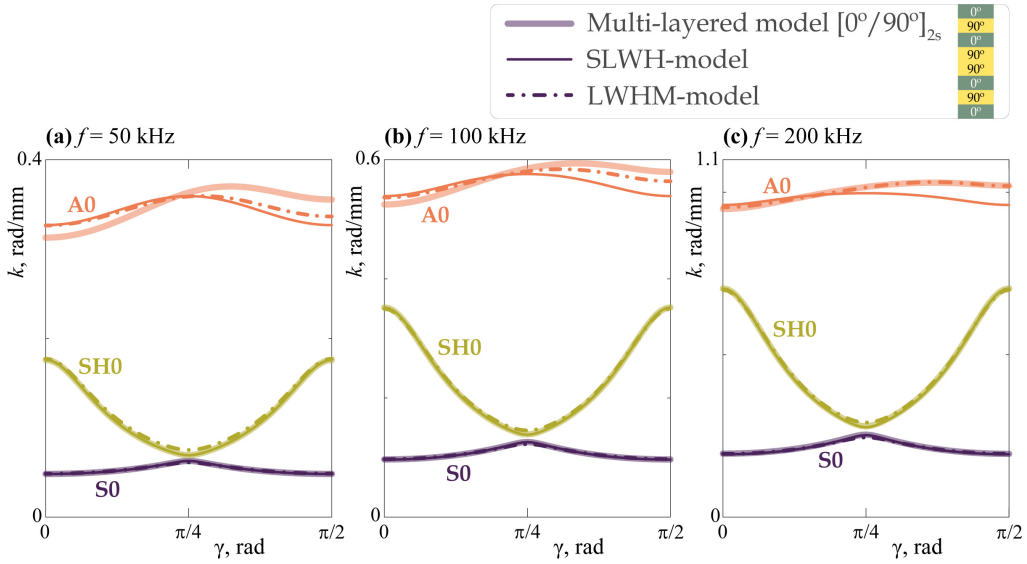


Figure 2. Wavenumbers $k_n(\gamma)$ for $[0°, 90°]_{2s}$: multi-layered waveguide (thick solid lines), homogenized waveguides (thin solid and dashed lines for Models 1 and 2, respectively).

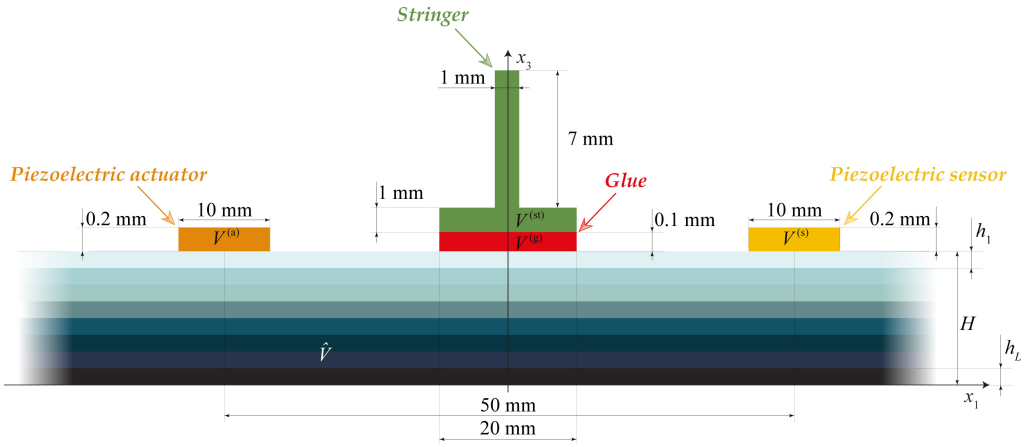


Figure 3. Geometry sketch of the considered plain-strain problem of EGW excitation, sensing, and scattering.

The governing equations for the time-harmonic motion of the piezoelectric media with the tensors of elastic, piezoelectric, dielectric constants $\hat{C}_{ijkl}$, $\hat{e}_{kij}$, $\hat{\varepsilon}_{ik}$ and mass density $\hat{\rho}$ can be written in terms of the displacement vector $\hat{\boldsymbol{u}}$ and the electric potential $\hat{\phi}$ [47]:

$$\hat{C}_{ijkl}\frac{\partial^2 \hat{u}_k(\boldsymbol{x})}{\partial x_l \partial x_j} + \hat{e}_{kij}\frac{\partial^2 \hat{\phi}(\boldsymbol{x})}{\partial x_k \partial x_j} + \hat{\rho}\omega^2 \hat{u}_i(\boldsymbol{x}) = 0, \tag{8}$$

$$\hat{e}_{ikl}\frac{\partial^2 \hat{u}_k(\boldsymbol{x})}{\partial x_l \partial x_i} - \hat{\varepsilon}_{ik}\frac{\partial^2 \hat{\phi}(\boldsymbol{x})}{\partial x_k \partial x_i} = 0. \tag{9}$$

The components of the electric field vector are the derivatives of the electric potential ϕ:

$$E_k = -\frac{\partial \phi}{\partial x_k}.$$

For the PWTs $\hat{V}^{(j)}$, the outer boundary $\partial\hat{V}^{(j)}$ is split into three parts $\partial\hat{V}^{(j)} = \hat{S}_{\mathrm{D}}^{(j)} \cup \hat{S}_{0}^{(j)} \cup \hat{S}_{\phi}^{(j)}$ in accordance with the boundary conditions. Lower surfaces of PWTs ($\hat{S}_{0}^{(j)} = \hat{V}^{(j)} \bigcap V, \quad j = \{\mathrm{a}, \mathrm{s}\}$) are assumed to be grounded, which means that electric potentials are equal zero

$$\hat{\phi}(\boldsymbol{x}, t) = 0, \qquad \boldsymbol{x} \in \hat{S}_{0}^{(j)}, \quad j = \{\mathrm{a}, \mathrm{s}\}. \tag{10}$$

An electric input impulse $p(t)$ with a given voltage φ_0 is applied at the second electroded surface $\hat{S}_{\phi}^{\mathrm{a}}$ of the piezoelectric actuator $\hat{V}^{(\mathrm{a})}$, is assumed to be known:

$$\hat{\phi}(\boldsymbol{x}, t) = \varphi_0 \cdot p(t), \qquad \boldsymbol{x} \in \hat{S}_{\phi}^{\mathrm{a}}, \quad t \geq t_0. \tag{11}$$

Zero electric displacements are assumed at the boundaries $\hat{S}_{\mathrm{D}}^{(j)}$ without electrodes

$$\hat{D}_{1}^{(j)}(\boldsymbol{x}) = 0, \quad \boldsymbol{x} \in \hat{S}_{\mathrm{D}}^{(j)}, \quad j = \{\mathrm{a}, \mathrm{s}\} \tag{12}$$

whereas electric potential at the grounded electrodes is assumed to be zero

$$\hat{\phi}^{(j)}(\boldsymbol{x}) = 0, \quad \boldsymbol{x} \in \hat{S}_{0}^{(j)}, \tag{13}$$

Electric potentials at electroded surfaces of sensor denoted is to be determined using two additional boundary conditions

$$\begin{aligned} &\hat{\phi}(\boldsymbol{x}) = \bar{\varphi}, \qquad \boldsymbol{x} \in \hat{S}_{\phi}^{\mathrm{s}}, \\ &\hat{Q}(\hat{\boldsymbol{u}}, \hat{\phi}) = \int\limits_{\hat{S}_{\phi}^{\mathrm{s}}} \hat{D}_2(\boldsymbol{x}) \mathrm{d}S = 0, \end{aligned} \tag{14}$$

where $\hat{Q}(\boldsymbol{u}, \phi)$ is the electric charge and the constant electric potential $\bar{\varphi}$ is assumed to be unknown. The continuity boundary conditions for the displacement and the traction vectors are also assumed in the contact area

$$u_i^{(L)}\Big|_{z=H} = \hat{u}_i^{(n)}\Big|_{z=H}, \quad \boldsymbol{\tau}_i^{(L)}\Big|_{z=H} = \hat{\boldsymbol{\tau}}_i^{(n)}\Big|_{z=H}, \quad n = \{\mathrm{a}, \mathrm{s}\} \tag{15}$$

and the stress free boundary conditions in $\hat{S}_{\mathrm{D}}^{(n)} \cup \hat{S}_{\phi}^{(n)}$. In the case of the stringer being glued at the surface of the laminate $\hat{V}$, two adjacent domains $V^{(\mathrm{g})}$ and $V^{(\mathrm{st})}$ describing respectively the glue layer and the T-shaped stringer are introduced as depicted in Figure 3. Since the stringer and the adhesive are elastic and isotropic, governing equation (2) reduced for isotropy are employed. The outer boundaries of $V^{(\mathrm{g})}$ and $V^{(\mathrm{st})}$ are stress-free, whereas the displacement and the traction vectors are assumed continuous at the interfaces $V \cap V^{(\mathrm{g})}$ and $V^{(\mathrm{g})} \cap V^{(\mathrm{st})}$ so that relations identical to (15) hold there.

To solve the formulated in-plane boundary value problem (1)–(3) together with (8)–(15), a recently developed SAHA has been employed. Its starting point is the integral representation describing wave fields induced due to the presence of PWTs and stringer, which is obtained form Equation (5) after its reduction to the plain-strain case:

$$\boldsymbol{u}^{(j)}(\boldsymbol{x}) = \frac{1}{2\pi} \int\limits_{\Gamma} \mathbf{K}^{(j)}(\alpha, x_3) \boldsymbol{Q}^{(j)}(\alpha) \mathrm{e}^{-\mathrm{i}\alpha x_1} \mathrm{d}\alpha, \quad j = \{\mathrm{a}, \mathrm{s}, \mathrm{st}\} \tag{16}$$

Here $\hat{\mathbf{K}}^{(j)}(\alpha, x_3)$ is the Fourier transform of the waveguide Green's matrix, $\boldsymbol{Q}^{(j)}(\alpha)$ is the Fourier transform of the unknown traction vector $\boldsymbol{q}^{(n)}(x_1)$ occurring in the second equality of (15) with respect to x_1 coordinate, while Γ is the integration contour in the complex plane α along the real axis surrounding poles of the integrand in accordance with the limiting absorption principle [39,40]. The surface-mounted PWATs are discretized using the frequency domain spectral element method (FDSEM) [48,49] using Lagrange interpo-

lation polynomials at the Gauss–Lobatto–Legendre point. Vectors $\boldsymbol{q}^{(n)}(x_1)$ are obtained from the coupled problem, where the displacement continuity at the interface between PWATs/stringer and the waveguide is assumed (first equality in Equation (15)). The latter is solved using Galerkin method by expanding the unknown traction vector using Lagrange interpolation polynomials at the Gauss–Lobatto–Legendre points. A detailed description of the SAHA could be found in Refs. [36,37].

3. Comparison of the Models

In this section, three aforementioned models for EGW phenomena simulation in a multi-layered composite are systematically compared. For this purpose, the same 8-layered symmetric laminate $[0°, 90°]_{2s}$ as described in Section 2.1.2 is considered. Owing to its symmetry properties, it is reduced to two plane-strain problems along planes $x_1 0 x_3$ and $x_2 0 x_3$ resulting in $[0°, 90°]_{2s}$ and $[90°, 0°]_{2s}$ laminates, respectively. The elastic constants of anisotropic plies as well as of corresponding homogenized layers which are required for plane-strain simulations [50] with respect to their orientation are summarized in Table 2. The material properties for PWTs that are employed for EGW excitation and sensing, as well as for the T-shaped stringer adhesively attached to the waveguide are provided in Tables 3 and 4, respectively.

Table 2. Elastic constants of anisotropic waveguides [GPa].

Material	C_{11}	C_{13}	C_{33}	C_{55}
0° ply	122.4	4.13	11.5	4.85
90° ply	11.5	6.47	11.5	2.51
Model 1, $x_1 0 x_3$ plane	67.0	5.30	11.5	3.31
Model 1, $x_2 0 x_3$ plane	67.0	5.30	11.5	3.31
Model 2, $x_1 0 x_3$ plane	64.8	3.63	11.1	3.39
Model 2, $x_2 0 x_3$ plane	64.8	3.90	11.1	2.85

Table 3. Material properties of PWT.

Material	Elastic Constants [GPa]	Piezoelectric Constants [C/m^2]	Dielectric Constants 10^{-9} [F/m]	Density [kg/m^3]
Piezoeletric material PWTs (PIC 155)	$C_{1111} = 120$ $C_{1112} = 67.1$ $C_{2222} = 94.2$ $C_{1212} = 22.3$	$e_{211} = -7.24$ $e_{212} = 13.77$ $e_{112} = 11.91$	$\varepsilon_{11} = 9.12$ $\varepsilon_{22} = 7.55$	7800

Table 4. Material properties of the stringer and adhesive.

Material	Young's Modulus [GPa]	Poisson's Ratio	Density [kg/m^3]
Aluminum (stringer)	70.0	0.33	2700
Adhesive	3.0	0.4	1248

3.1. EGW Dispersion Characteristics

First, let us compare the dispersion characteristics of the 8-layered anisotropic symmetric laminate and two homogenized single layer waveguides, which properties are determined using the SLWH-model and the LWHM-model described in Section 2.1.2. Figures 4 and 5 depict the slownesses $s_n(f)$ of EGWs propagating for two orthogonal orientations of the considered composite, i.e., $[0°, 90°]_{2s}$ and $[90°, 0°]_{2s}$. One can see that for the first of them both homogenized models provide similar results and are capable

to predict adequately the behavior of fundamental and high-order antisymmetric waves in a multilayered waveguide including the values of their cut-off frequencies. The particular benefit of LWHM-model here is that for $A0$ mode the dispersion curve evaluated with it is closer to the results of the complete multi-layered model than the one obtained with the SLWH-model. For symmetric modes, good coincidence between multi-layered and homogenized models is observed only for $S0$ mode and for the frequency range where it is almost non-dispersive, i.e., up to $f = 400$ kHz. With the increasing frequency, not only the particular trajectories of $s_n(f)$ for symmetric modes become dissimilar but the values of cut-off frequencies are also not properly addressed (e.g., for $S2$ mode).

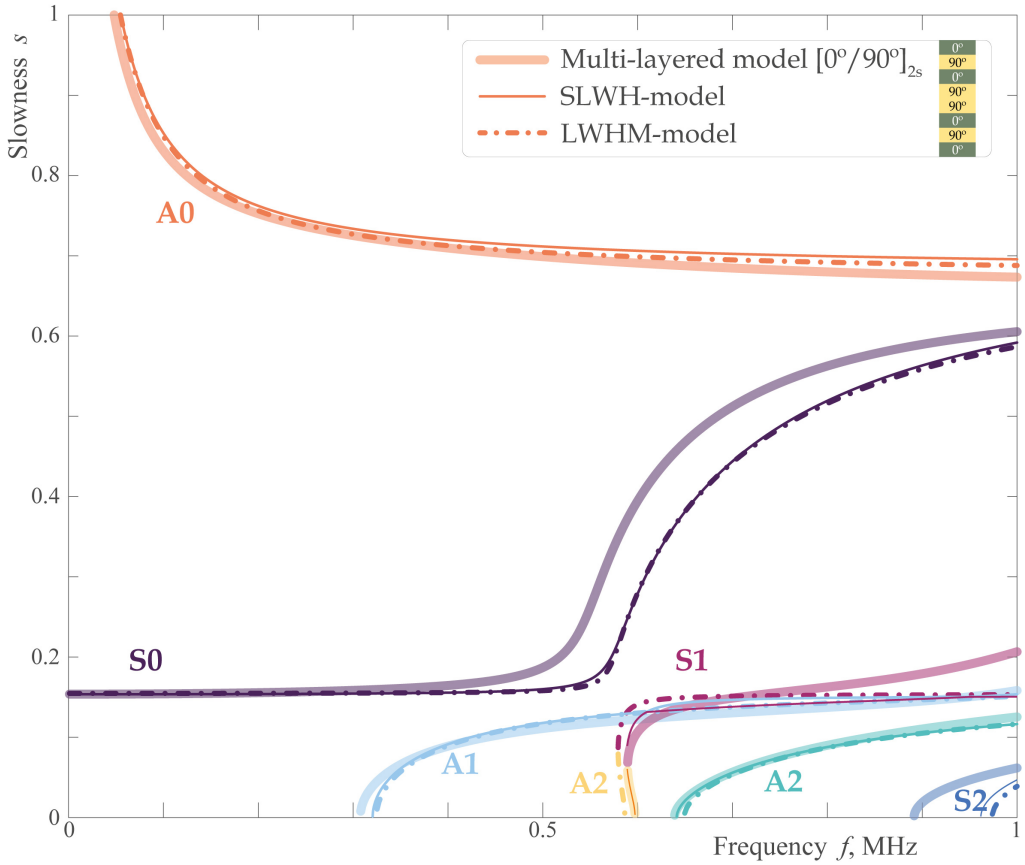


Figure 4. Slownesses $s_n(f)$ for $[0°, 90°]_{2s}$: multi-layered waveguide (thick solid lines), homogenized waveguides (dashed and thin solid lines).

For $[90°, 0°]_{2s}$ waveguide, the obtained results are somewhat different. In general, the discrepancies between multilayered and homogenized models have increased. Although LWHM-model for $A0$ mode in the frequency range below 500 kHz outperforms the SLWH one, for higher frequencies, on the contrary, SLWH $s_{A0}(f)$ curve is closer to results evaluated with the multilayered model. Moreover, the values of cut-off frequencies for $A1$ and $A2$ modes predicted with SLWH deviate stronger from original data than those obtained with SLWH-model. It is interesting to note that for the frequency range when $S0$ mode becomes dispersive, the LWHM-curve is notably closer to the results of the multilayered model.

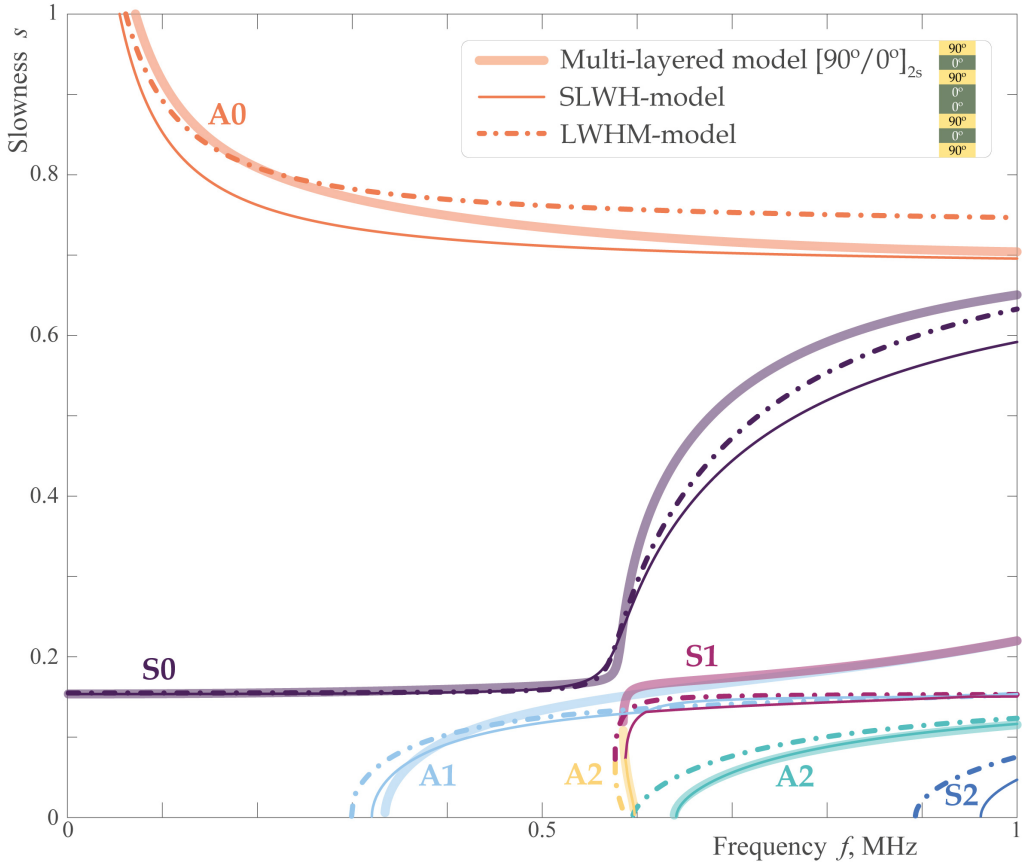


Figure 5. Slownesses $s_n(f)$ for $[90°, 0°]_{2s}$: multi-layered waveguide (thick solid lines), homogenized waveguides (dashed and thin solid lines).

Some of the aforementioned observations could be explained by comparing corresponding normal mode eigenforms. Figures 6–9 demonstrate eigenforms (energy flow e_1 along the horizontal coordinate axis, vertical and horizontal displacements u_k) calculated via the multi-layered and SLWH models. Here normalized values $\tilde{u}_k(x_3)$ and $\tilde{e}_1(x_3)$ for each frequency are shown, where $\tilde{u}_k(x_3)$ is normalized for each frequency by the maximum value of the displacement vector at frequency f over the waveguide $\max_{x_3} |\boldsymbol{u}(x_3)|$ and $e_1(x_3)$ is normalized by the value $\max_{x_3} |\boldsymbol{e}_1(x_3)|$. The time-averaged power density vector $\boldsymbol{e}(\boldsymbol{x})$ or Umov–Poynting vector is evaluated as follows:

$$e_j = \frac{\omega}{2} \operatorname{Im}(\sigma_{1j} u_1^* + \sigma_{3j} u_3^*).$$

The eigenforms calculated employing two approaches for two fundamental and two first higher-order modes have been analyzed. Similarly to the results presented in Figures 4 and 5, the analysis reveals good agreement between models at lower frequencies for $A0$ and $S0$ modes, whereas the discrepancy increases with the frequency growth for both orientations. A closer look at Figures 8 and 9 could explain the results regarding dispersion curves of high-order $A1$ and $S1$ modes. In particular, comparing horizontal and vertical eigenform components (subplots a,b and d,e) in Figure 8, the good coincidence between the multilayered and SLWH model results for $[0°, 90°]_{2s}$ waveguides are observed, which is also noted for $A1$ dispersion curve in Figure 4. At the same time, for $[90°, 0°]_{2s}$ laminate discrepancies in u_1 and u_3 are more pronounced and as could be seen from Figure 5, both homogenized models do not catch the trajectory of $s_{A1}(f)$, especially for higher value of f. For $S1$ mode, a certain coincidence in eigenforms could be observed only for $[0°, 90°]_{2s}$ waveguide at the vicinity of $f = 600$ kHz and the analogous behavior is noted in Figure 4.

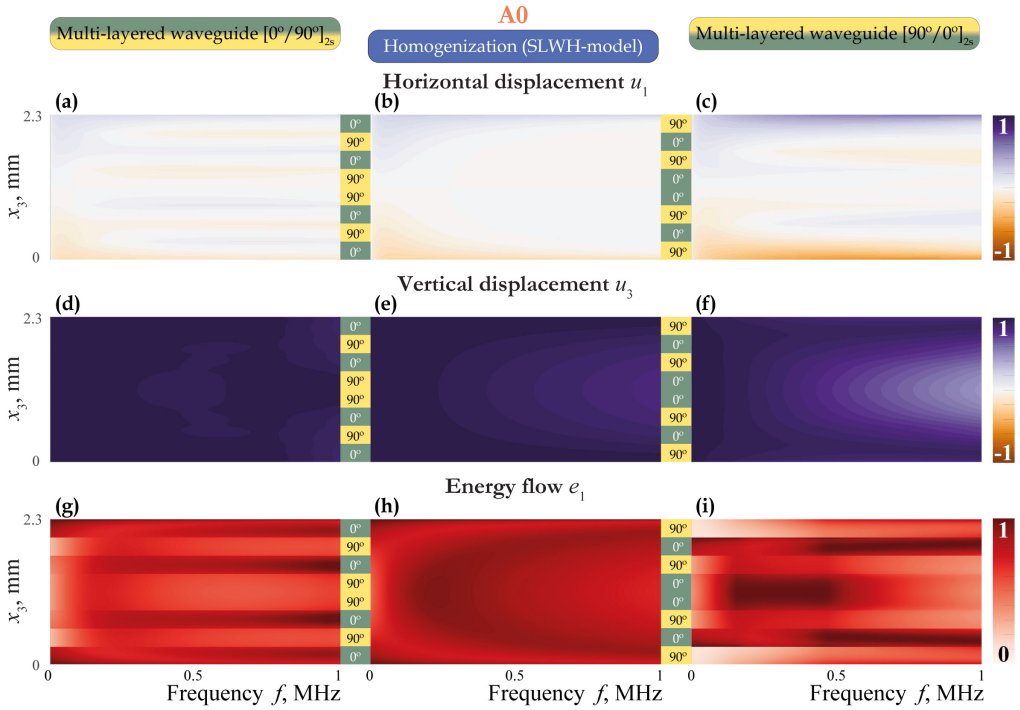


Figure 6. Eigenforms for the first fundamental guided wave A0 propagating in multi-layered waveguide $[0°, 90°]_{2s}$ (**a**,**d**,**g**), homogeneous waveguide according to the SLWH-model (**b**,**e**,**h**) and multi-layered waveguide $[90°, 0°]_{2s}$ (**c**,**f**,**i**).

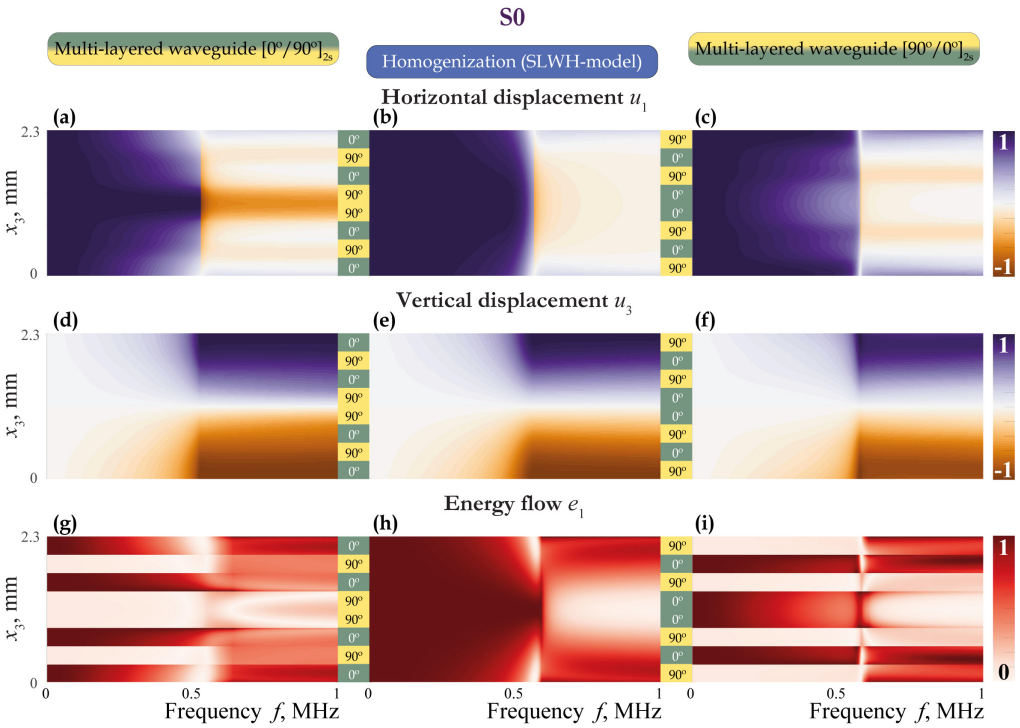


Figure 7. Eigenforms for the first fundamental guided wave S0 propagating in multi-layered waveguide $[0°, 90°]_{2s}$ (**a**,**d**,**g**), homogeneous waveguide according to the SLWH-model (**b**,**e**,**h**), and multi-layered waveguide $[90°, 0°]_{2s}$ (**c**,**f**,**i**).

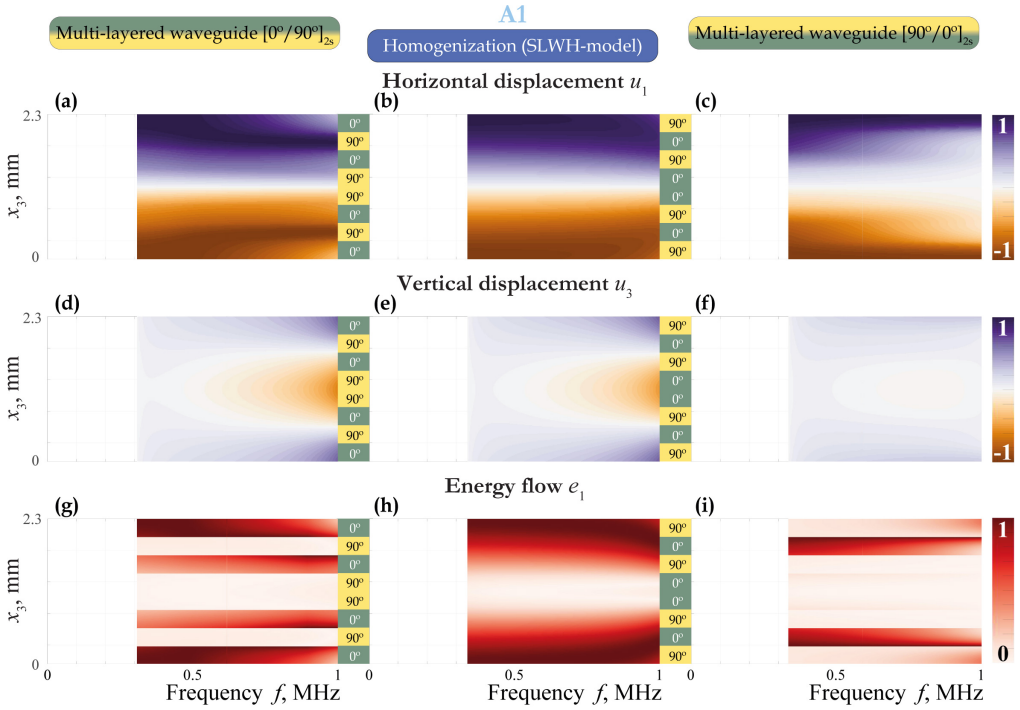


Figure 8. Eigenforms for the guided wave A1 propagating in multi-layered waveguide $[0°, 90°]_{2s}$ (**a**,**d**,**g**), homogeneous waveguide according to the SLWH-model (**b**,**e**,**h**), and multi-layered waveguide $[90°, 0°]_{2s}$ (**c**,**f**,**i**).

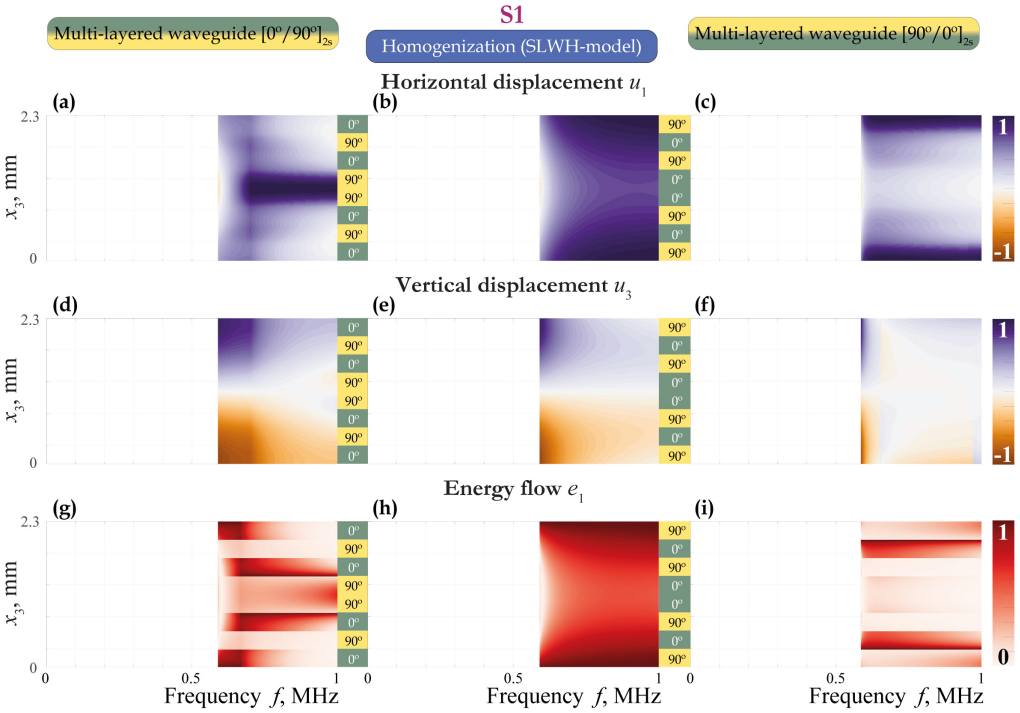


Figure 9. Eigenforms for the first fundamental guided wave S1 propagating in multi-layered waveguide $[0°, 90°]_{2s}$ (**a**,**d**,**g**), homogeneous waveguide according to the SLWH-model (**b**,**e**,**h**), and multi-layered waveguide $[90°, 0°]_{2s}$ (**c**,**f**,**i**).

As expected, the distribution of the power density over the cross-section of the waveguide differs more for all the normal modes considered due to its dependency on the components of the stress tensor, which is greater in sub-layers with 0° orientation of fibers.

3.2. Excitation of EGWs

As a starting point, the accuracy of the SAHA in the case of an anisotropic waveguide is illustrated. Figure 10 demonstrates total displacement amplitudes calculated for $[0°, 90°]_{2s}$ composite using the SAHA with different number N_e of elements discretizing the PWTs along x_1-axis and the conventional FEM (COMSOL Multiphysics 6.0; COMSOL AB, Stockholm, Sweden). In the latter, perfectly matched layers are employed to simulate an infinite waveguide, and 2,083,295 degrees of freedom (DoF) in total have been used with quintic polynomial approximation. Such a big amount of DoF is conditioned by the fact that each sublayer was discretized at least with three FE along its thickness, and very fine mesh in the contact areas between the PWTs and the waveguide was employed. Here and further on for the numerical results presented, PWTs of length $a = 10$ mm and thickness $d = 0.2$ mm with mechanical and piezoelectric properties listed in Table 3 have been used (both for the actuator and sensor). One can see that only $N_e = 10$ of elements are enough in the SAHA to achieve a good accuracy.

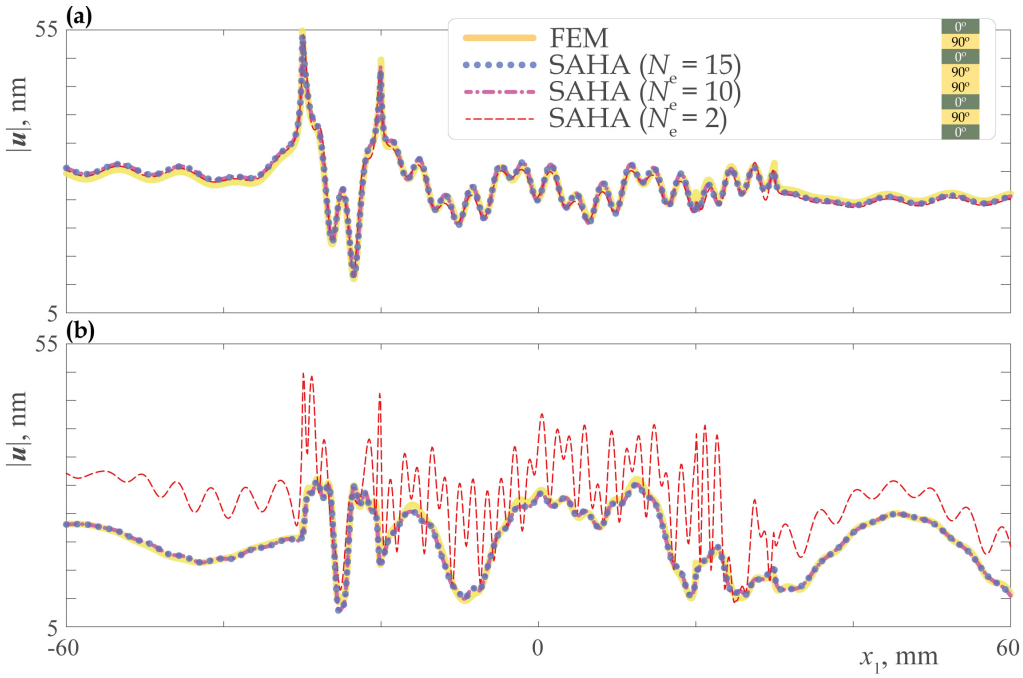


Figure 10. Displacement amplitudes $|\boldsymbol{u}|(x_1, 0)$ on the surface of multi-layered waveguide $[0°, 90°]_{2s}$ with an actuator and a sensor at frequencies $f = 200$ kHz (**a**) and $f = 400$ kHz (**b**).

In Table 5, the computational times required to obtain the results from Figure 10 employing a multi-layered model are presented. For comparison, analogous values when the waveguide is simulated with the SLWH model are also provided (the corresponding COMSOL model consists of 518,745 DoF). The calculations have been performed using a custom work station equipped with Intel Xeon CPU E5-2660 v4 and 240 GB of RAM. Only a single CPU-core is employed by the SAHA program code ($N_e = 10$ elements), while all 14 physical CPU-cores are utilized by COMSOL. Table 5 illustrates the fact that the employment of the single layer model sufficiently reduces the computational costs.

The SAHA allows for investigating the elastic wave energy transfer from the source of motion into the elastic structure. The wave energy transferred into the laminated structure due to the action of the PWT $\hat{V}^{(a)}$ is calculated in terms of the vertical component e_2 of the time-averaged power density vector (see Ref. [37]):

$$E_0 = \int\limits_{S_0^{(a)}} e_2(x_1, H) \mathrm{d}x_1. \tag{17}$$

Table 5. Computational times for the waveguide $[0°, 90°]_{2s}$ with two PWTs, in seconds.

	SAHA, $N_e = 10$ (1 Core), s	**FEM (COMSOL) (14 Cores), s**
	f = 200 kHz	
SLWH	40	51
Multi-layered $[0°, 90°]_{2s}$	182	161
	f = 400 kHz	
SLWH	37	51
Multi-layered $[0°, 90°]_{2s}$	170	161

Corresponding values of $E_0(f)$ induced by the piezoelectric actuator mounted on the surface of the multi-layered waveguide are shown in Figures 11 and 12 for $[0°, 90°]_{2s}$ and $[90°, 0°]_{2s}$, respectively. For both waveguides, the results provided by homogenized models are comparable with the data from the multilayered one up to the frequency $f = 500$ kHz. Moreover, when $f < 200$ kHz, good quantitative coincidence is also observed for the $[0°, 90°]_{2s}$ laminate. At the same time, for $[90°, 0°]_{2s}$ structure, $E_0(f)$ curve evaluated with the LWHM-model is closer to the one obtained with the multilayered model, although, in general, the discrepancy is higher.

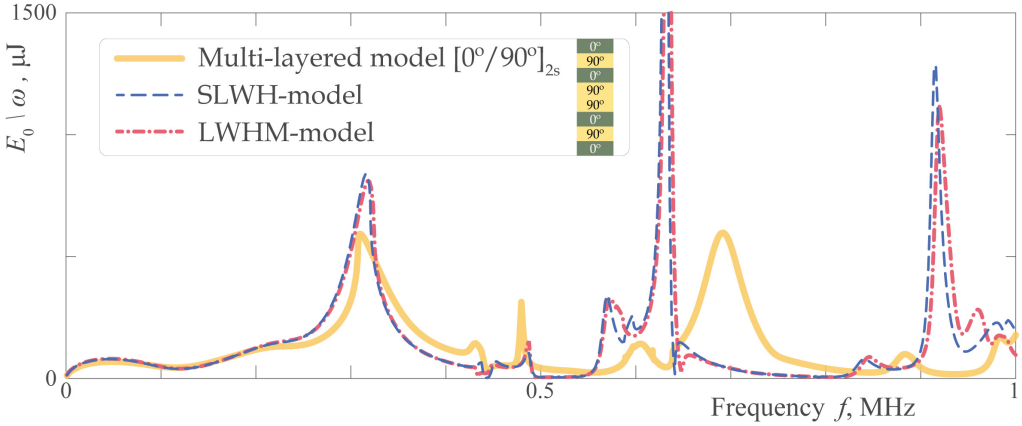


Figure 11. The wave energy transferred into the waveguide $E_0(f)$ by the PWT on the surface of multi-layered waveguide $[0°, 90°]_{2s}$ (thick solid line), and waveguides with effective properties estimated according to the SLWH-model (thin solid line) and the LWHM-model (dash-dotted line).

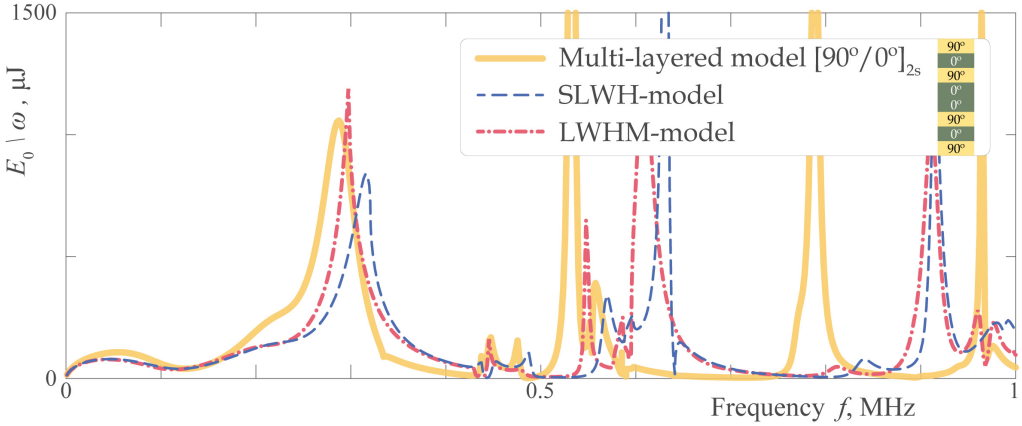


Figure 12. The wave energy transferred into the waveguide $E_0(f)$ by the PWT on the surface of multi-layered waveguide $[90°, 0°]_{2s}$ (thick solid line), and waveguides with effective properties estimated according to the SLWH-model (thin solid line) and the LWHM-model (dash-dotted line).

3.3. Sensing and Scattering of EGWs

Figures 13–16 show the response of the piezoelectric sensor to guided waves excited by the actuator for the considered models. The first two are obtained for an intact structure, while Figures 15 and 16 are calculated for a waveguide with a T-shaped stringer adhesively attached to its upper surface $x_3 = H$ (geometric parameters of this obstacle and adhesive are provided in Figure 3, while their mechanical properties are summarized in Table 4). As in the previous cases, the models are in qualitative agreement with each other at lower frequencies. When, however, $\bar{\varphi}(f)$ is quantitatively compared, acceptable results for the waveguide $[90°, 0°]_{2s}$ are obtained in a rather narrow frequency range (below 20 kHz) while for the $[0°, 90°]_{2s}$ laminate it is wider (below 200 kHz) (zoomed parts in Figures 13 and 14). If the scattering by the stringer is additionally considered, the coincidence of the homogenized models with the multi-layered laminate model is mainly qualitative, but not quantitative. Here again, the LWHM-model predicts the dynamics of the laminate more accurately than the SLWH-model. The values and local maxima of the voltage $\bar{\varphi}(f)$ measured via the sensor are shown in Figures 15 and 16 (up to 400 kHz for $[0°, 90°]_{2s}$ and $[90°, 0°]_{2s}$ waveguides).

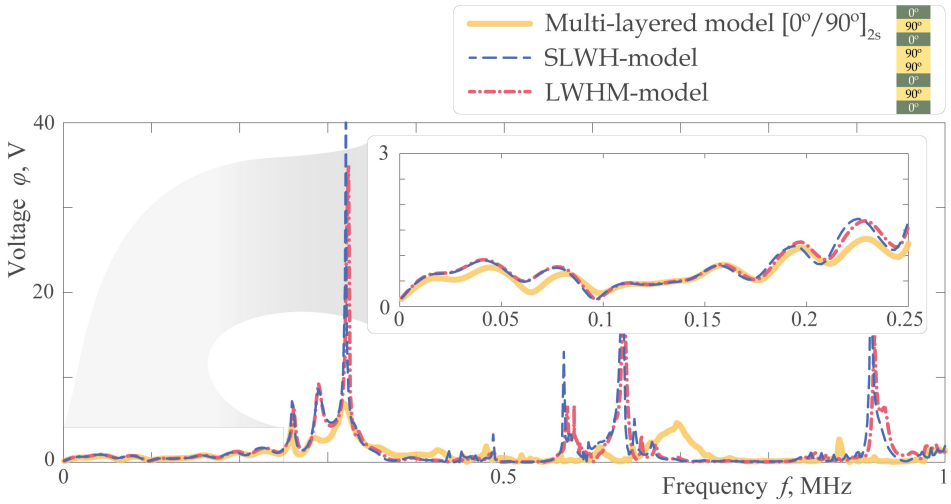


Figure 13. Voltage $\bar{\varphi}(f)$ measured at the sensor on the surface of multi-layered waveguide $[0°, 90°]_{2s}$ (thick solid line), and waveguides with effective properties estimated according to the SLWH-model (thin solid line) and the LWHM-model (dash-dotted line).

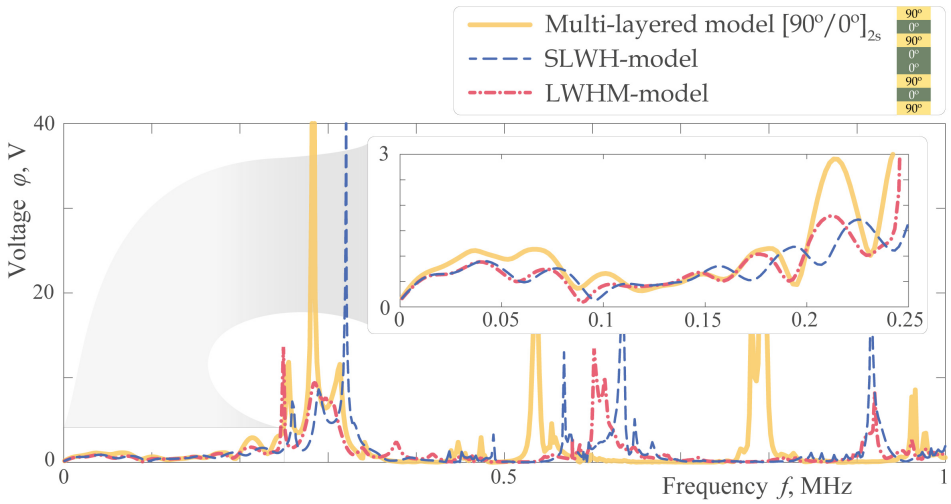


Figure 14. Voltage $\bar{\varphi}(f)$ measured at the sensor on the surface of multi-layered waveguide $[90°, 0°]_{2s}$ (thick solid line), and waveguides with effective properties estimated according to the SLWH-model (thin solid line) and the LWHM-model (dash-dotted line).

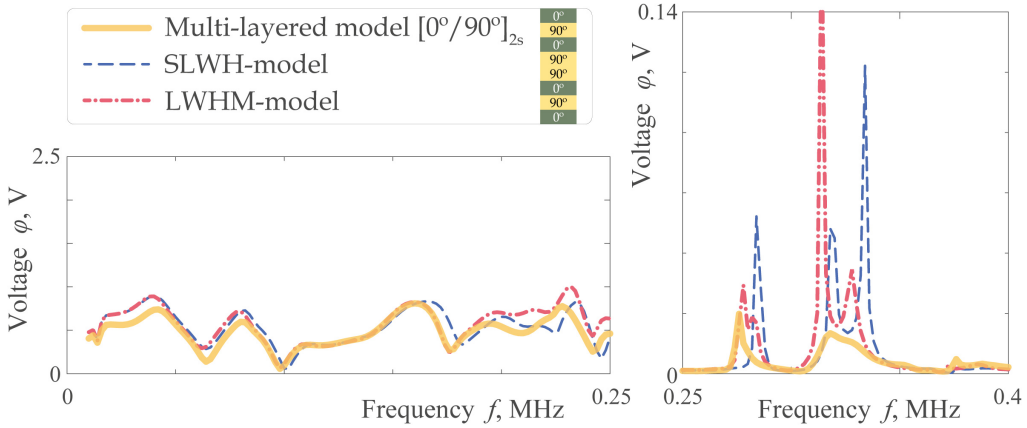


Figure 15. Voltage $\bar{\varphi}(f)$ measured at the sensor on the surface of the multi-layered waveguide $[90°, 0°]_{2s}$ (thick solid line), and waveguides with effective properties estimated according to the SLWH-model (thin solid line) and the LWHM-model (dash-dotted line) in the case of the surface-mounted stringer.

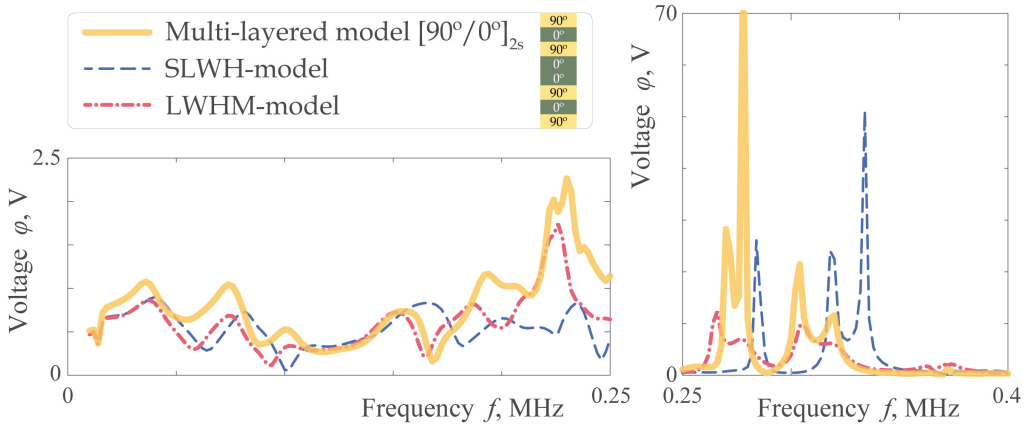


Figure 16. Voltage $\bar{\varphi}(f)$ measured at the sensor on the surface of the multi-layered waveguide $[0°, 90°]_{2s}$ (thick solid line), and waveguides with effective properties estimated according to the SLWH-model (thin solid line) and the LWHM-model (dash-dotted line) in the case of the surface-mounted stringer.

4. Discussion

The configuration and optimization of guided wave-based NDT/SHM systems is still a challenging task that requires extensive and time-consuming numerical simulations, especially when complex wave phenomena in composite structures incorporating constructive irregularities and/or defects as well as a set of installed sensors are considered, e.g., see Ref. [19]. Therefore, it is a natural temptation to replace complex multi-layered laminates with an effective single layer in order to cut down computational costs in the numerics. The application of such an approach for EGW phenomena simulations might be particularly beneficial when standard FEM codes are employed, since no specific modification to the FEM-based evaluations are required. The results presented in the current paper demonstrate, however, that the researchers should be careful when applying such effective models for simulating guided waves propagation and scattering in anisotropic multi-layered composites with PWTs and inhomogeneities.

Within this study, two approaches for the evaluation of the elastic properties of such effective single layer are implemented, namely, SLWH and LWHM models. In the first one, the corresponding stiffness matrix $\bar{C}_{ij}$ is directly related to the sublayers' elastic properties through the Equation (6). However, this approach does not take into account the peculiarities of the composite stacking sequence, i.e., identical matrices $\bar{C}_{ij}$ would be obtained either for symmetric or non-symmetric balanced cross-ply laminates with $\bar{C}_{11} = \bar{C}_{22}$

and $\bar{C}_{44} = \bar{C}_{55}$. Since these equalities hold, the SLWH model is not capable of tackling the difference between EGW dispersion properties for 0° and 90° propagation directions typical for symmetric cross-ply composites [51]. In the proposed LWHM approach, this issue is addressed by evaluating $\bar{C}_{ij}$ through the optimization problem where angular dependencies of EGW dispersion curves solve as an input. However, their preliminary calculation is required and the solution of the corresponding minimization problem (7) should be performed.

With the provided numerical results, it is illustrated that effective single layer models cannot exactly predict the dynamic behavior of symmetric cross-ply laminates fabricated from unidirectional prepregs. Even for the fundamental $A0$ mode, its dispersion properties evaluated within SLWH and LWHM models and multi-layered model differ for the orientation 90° related to the plane-strain problem for $[90°, 0°]_{2s}$ sample. If the pair of PWTs, i.e., actuator/sensor, mounted on the surface of an 8-layered symmetric laminate is considered, both effective models give results that are qualitatively similar to the multi-layered model only at low frequencies (approximately up to 150–200 kHz). The discrepancy becomes larger and the frequency range, where the effective models are valid, decreases if the T-shaped stringer is glued on the surface of the laminated structure. The reason is naturally revealed: differences in sensor response evaluated either with single layer models or for the initial multilayered structure both for intact waveguide or a laminate with a surface-mounted stringer could be explained by the fact that in the homogenized models the information about the stiffness of the upper sub-layer is smeared through the whole thickness of the waveguide. This parameter is essential for the quantitative evaluation of the energy transfer along the composite, ultimately affecting output voltages from the sensor, especially when a surface obstacle is present.

As a trade-off between computational costs and the higher simulation adequacy of homogenized models, it might be suggested to introduce a partial reduction of an initially multilayered structure to a set of unified cells, each of which, in turn, is further homogenized and, therefore, substituted by a single layer with effective mechanical properties. Such a procedure would reduce the total number of layers and keep more information regarding the physics of EGWs in a composite. Its practical implementation along with the generalization of the obtained results for a more complex complete three-dimensional problem would be the topics of further research activities.

Author Contributions: Conceptualization, A.A.E. (Artem A. Eremin) and M.V.G.; methodology, A.A.E. (Artem A. Eremin), M.V.G. and S.I.F.; software, S.I.F., A.A.E. (Alexander A. Evdokimov) and P.A.N.; validation, M.V.G., S.I.F. and A.A.E. (Alexander A. Evdokimov); formal analysis, A.A.E. (Artem A. Eremin), and M.V.G.; investigation, A.A.E. (Artem A. Eremin), M.V.G., S.I.F., A.A.E. (Alexander A. Evdokimov) and P.A.N.; resources, A.A.E. (Artem A. Eremin); data curation, S.I.F., A.A.E. (Alexander A. Evdokimov) and P.A.N.; writing—original draft preparation, A.A.E. (Artem A. Eremin), M.V.G., S.I.F. and A.A.E. (Alexander A. Evdokimov); writing—review and editing, A.A.E. (Artem A. Eremin), M.V.G. and S.I.F.; visualization, M.V.G.; project administration, A.A.E. (Artem A. Eremin). All authors have read and agreed to the published version of the manuscript.

Funding: This research was funded by the Ministry of Science and Higher Education of the Russian Federation (Project No FZEN-2020-0017).

Institutional Review Board Statement: Not applicable.

Data Availability Statement: Not applicable.

Acknowledgments: The authors are grateful to the members of the DFG Scientific Network "Towards a holistic quality assessment for guided wave-based SHM": Inka Mueller, Vittorio Memmolo, Kilian Tschöke, Maria Moix-Bonet, Yevgeniya Lugovtsova, Jochen Moll, Ramanan Venkat for the fruitful discussions that initiated the present investigation.

Conflicts of Interest: The authors declare no conflict of interest.

References

1. Irving, P.; Soutis, C. (Eds.) *Polymer Composites in the Aerospace Industry*; Elsevier: Amsterdam, The Netherlands, 2020. [CrossRef]
2. Mishnaevsky, L.; Branner, K.; Petersen, H.N.; Beauson, J.; McGugan, M.; Sorensen, B.F. Materials for Wind Turbine Blades: An Overview. *Materials* **2017**, *10*, 1285. [CrossRef]
3. He, C.; Yu, R.; Sun, H.; Chen, Z. Lightweight multilayer composite structure for hydrogen storage tank. *Int. J. Hydrogen Energy* **2016**, *41*, 15812–15816. [CrossRef]
4. Elsheikh, A. Bistable Morphing Composites for Energy-Harvesting Applications. *Polymers* **2022**, *14*, 1893. [CrossRef]
5. Rajak, D.K.; Pagar, D.D.; Kumar, R.; Pruncu, C.I. Recent progress of reinforcement materials: A comprehensive overview of composite materials. *J. Mater. Res. Technol.* **2019**, *8*, 6354–6374. [CrossRef]
6. Anand Raj, M.K.; Muthusamy, S.; Panchal, H.; Mahmoud Ibrahim, A.M.; Alsoufi, M.S.; Elsheikh, A.H. Investigation of mechanical properties of dual-fiber reinforcement in polymer composite. *J. Mater. Res. Technol.* **2022**, *18*, 3908–3915. [CrossRef]
7. Wang, B.; Zhong, S.; Lee, T.L.; Fancey, K.S.; Mi, J. Non-destructive testing and evaluation of composite materials/structures: A state-of-the-art review. *Adv. Mech. Eng.* **2020**, *12*, 1687814020913761. [CrossRef]
8. Güemes, A.; Fernandez-Lopez, A.; Pozo, A.R.; Sierra-Perez, J. Structural Health Monitoring for Advanced Composite Structures: A Review. *J. Compos. Sci.* **2020**, *4*, 13. [CrossRef]
9. Mitra, M.; Gopalakrishnan, S. Guided wave based structural health monitoring: A review. *Smart Mater. Struct.* **2016**, *25*, 53001. [CrossRef]
10. Ricci, F.; Monaco, E.; Boffa, N.; Maio, L.; Memmolo, V. Guided waves for structural health monitoring in composites: A review and implementation strategies. *Prog. Aerosp. Sci.* **2022**, *129*, 100790. [CrossRef]
11. Humeida, Y.; Pinfield, V.J.; Challis, R.E.; Wilcox, P.D.; Li, C. Simulation of ultrasonic array imaging of composite materials with defects. *IEEE Trans. Ultrason. Ferroelectr. Freq. Control.* **2013**, *60*, 1935–1948. [CrossRef] [PubMed]
12. Glushkov, E.; Glushkova, N.; Eremin, A.; Lammering, R.; Neumann, M. Frequency dependent directivity of guided waves excited by circular transducers in anisotropic composite plates. *J. Acoust. Soc. Am.* **2012**, *132*, EL119–EL124. [CrossRef] [PubMed]
13. Yu, X.; Ratassepp, M.; Rajagopal, P.; Fan, Z. Anisotropic effects on ultrasonic guided waves propagation in composite bends. *Ultrasonics* **2016**, *72*, 95–105. [CrossRef] [PubMed]
14. Shen, Y.; Cesnik, C.E.S. Hybrid local FEM/global LISA modeling of damped guided wave propagation in complex composite structures. *Smart Mater. Struct.* **2016**, *25*, 95021. [CrossRef]
15. Castaings, M.; Singh, D.; Viot, P. Sizing of impact damages in composite materials using ultrasonic guided waves. *NDT E Int.* **2012**, *46*, 22–31. [CrossRef]
16. Liu, Y.; Hong, X.; Zhang, B. A novel velocity anisotropy probability imaging method using ultrasonic guided waves for composite plates. *Measurement* **2020**, *166*, 108087. [CrossRef]
17. Kudela, P.; Radzienski, M.; Ostachowicz, W. Impact induced damage assessment by means of Lamb wave image processing. *Mech. Syst. Signal Process.* **2018**, *102*, 23–36. [CrossRef]
18. Yang, C.; Liang, K.; Zhang, X.; Geng, X. Sensor placement algorithm for structural health monitoring with redundancy elimination model based on sub-clustering strategy. *Mech. Syst. Signal Process.* **2019**, *124*, 369–387. [CrossRef]
19. Mueller, I.; Memmolo, V.; Tschöke, K.; Moix-Bonet, M.; Möllenhoff, K.; Golub, M.V.; Venkat, R.S.; Lugovtsova, Y.; Eremin, A.A.; Moll, J. Performance Assessment for a Guided Wave-Based SHM System Applied to a Stiffened Composite Structure. *Sensors* **2022**, *22*, 7529. [CrossRef]
20. Maio, L.; Fromme, P. On ultrasound propagation in composite laminates: Advances in numerical simulation. *Prog. Aerosp. Sci.* **2022**, *129*, 100791. [CrossRef]
21. De Luca, A.; Perfetto, D.; De Fenza, A.; Petrone, G.; Caputo, F. Guided waves in a composite winglet structure: Numerical and experimental investigations. *Compos. Struct.* **2019**, *210*, 96–108. [CrossRef]
22. Voß, M.; Ilse, D.; Hillger, W.; Vallee, T.; Eppmann, M.; de Wit, J.; von Dungern, F. Numerical simulation of the propagation of Lamb waves and their interaction with defects in C-FRP laminates for non-destructive testing. *Adv. Compos. Mater.* **2020**, *29*, 423–441. [CrossRef]
23. Leckey, C.A.; Wheeler, K.R.; Hafiychuk, V.N.; Hafiychuk, H.; Timucin, D.A. Simulation of guided-wave ultrasound propagation in composite laminates: Benchmark comparisons of numerical codes and experiment. *Ultrasonics* **2018**, *84*, 187–200. [CrossRef] [PubMed]
24. Kudela, P.; Moll, J.; Fiborek, P. Parallel spectral element method for guided wave based structural health monitoring. *Smart Mater. Struct.* **2020**, *29*, 95010. [CrossRef]
25. Kudela, P.; Zak, A.; Krawczuk, M.; Ostachowicz, W. Modelling of wave propagation in composite plates using the time domain spectral element method. *J. Sound Vib.* **2007**, *302*, 728–745. [CrossRef]
26. Willberg, C.; Duczek, S.; Vivar Perez, J.; Schmicker, D.; Gabbert, U. Comparison of different higher order finite element schemes for the simulation of Lamb waves. *Comput. Methods Appl. Mech. Eng.* **2012**, *241–244*, 246–261. [CrossRef]
27. Maio, L.; Memmolo, V.; Ricci, F.; Boffa, N.; Monaco, E.; Pecora, R. Ultrasonic wave propagation in composite laminates by numerical simulation. *Compos. Struct.* **2015**, *121*, 64–74. [CrossRef]
28. Nanda, N.; Kapuria, S.; Gopalakrishnan, S. Spectral finite element based on an efficient layerwise theory for wave propagation analysis of composite and sandwich beams. *J. Sound Vib.* **2014**, *333*, 3120–3137. [CrossRef]

29. Orta, A.H.; Vandendriessche, J.; Kersemans, M.; Van Paepegem, W.; Roozen, N.B.; Van Den Abeele, K. Modeling lamb wave propagation in visco-elastic composite plates using a fifth-order plate theory. *Ultrasonics* **2021**, *116*, 106482. [CrossRef] [PubMed]
30. Chou, P.; Carleone, J.; Hsu, C. Elastic Constants of Layered Media. *J. Compos. Mater.* **1972**, *6*, 80–93. [CrossRef]
31. Sun, C.; Li, S. Three-Dimensional Effective Elastic Constants for Thick Laminates. *J. Compos. Mater.* **1988**, *22*, 629–639. [CrossRef]
32. Whitcomb, J.; Noh, J. Concise Derivation of Formulas for 3D Sublaminate Homogenization. *J. Compos. Mater.* **2000**, *34*, 522–535. [CrossRef]
33. Wang, L.; Rokhlin, S.I. Floquet wave homogenization of periodic anisotropic media. *J. Acoust. Soc. Am.* **2002**, *112*, 38–45. [CrossRef]
34. Karunasena, W.; Shah, A.H.; Datta, S.K. Wave Propagation in a Multilayered Laminated Cross-Ply Composite Plate. *J. Appl. Mech.* **1991**, *58*, 1028–1032. [CrossRef]
35. Datta, S.; Ju, T.H.; Bratton, R.; Shah, A. Transient response of a laminated composite plate: Results from homogenization and discretization. *Int. J. Solids Struct.* **1992**, *29*, 1711–1721. [CrossRef]
36. Golub, M.V.; Shpak, A.N. Semi-analytical hybrid approach for the simulation of layered waveguide with a partially debonded piezoelectric structure. *Appl. Math. Model.* **2019**, *65*, 234–255. [CrossRef]
37. Golub, M.V.; Eremin, A.A.; Shpak, A.N.; Lammering, R. Lamb wave scattering, conversion and resonances in an elastic layered waveguide with a surface-bonded rectangular block. *Appl. Acoust.* **2019**, *155*, 442–452. [CrossRef]
38. Golub, M.V.; Shpak, A.N.; Mueller, I.; Fomenko, S.I.; Fritzen, C.P. Lamb wave scattering analysis for interface damage detection between a surface-mounted block and elastic plate. *Sensors* **2021**, *21*, 1–25. [CrossRef]
39. Sveshnikov, A.G. The limit absorption principle for a waveguide. *Dokl. Akad. Nauk. USSR* **1951**, *80*, 345–347.
40. Glushkov, E.V.; Glushkova, N.V. On the efficient implementation of the integral equation method in elastodynamics. *J. Comput. Acoust.* **2001**, *9*, 889–898. [CrossRef]
41. Glushkov, E.; Glushkova, N.; Eremin, A. Forced wave propagation and energy distribution in anisotropic laminate composites. *J. Acoust. Soc. Am.* **2011**, *129*, 2923–2934. [CrossRef]
42. Nayfeh, A.H. *Wave Propagation in Layered Anisotropic Media with Applications to Composites*; Elsevier Academic Press: Amsterdam, The Netherlands, 1995; p. 696.
43. Lu, L.; Charron, E.; Glushkov, E.; Glushkova, N.; Bonello, B.; Julien, F.H.; Gogneau, N.; Tchernycheva, M.; Boyko, O. Probing elastic properties of nanowire-based structures. *Appl. Phys. Lett.* **2018**, *113*, 161903. [CrossRef]
44. Golub, M.V.; Doroshenko, O.V.; Arsenov, M.; Bareiko, I.; Eremin, A.A. Identification of material properties of elastic plate using guided waves based on the matrix pencil method and laser Doppler vibrometry. *Symmetry* **2022**, *14*, 1077. [CrossRef]
45. Krishnakumar, K. Micro-genetic algorithms for stationary and non-stationary function optimization. In *Intelligent Control and Adaptive Systems*; Rodriguez, G., Ed.; International Society for Optics and Photonics: Philadelphia, PA, USA, 1990; Volume 1196, pp. 289–296. [CrossRef]
46. Eremin, A.; Miakisheva, O.; Glushkov, E.; Glushkova, N.; Lammering, R. Advanced characterization of laminate fiber-reinforced composite materials with elastic guided waves and non-contact measurement techniques. In *Advanced Materials: Techniques, Physics, Mechanics and Applications*; Parinov, I.A., Chang, S.H., Jani, M.A., Eds.; Springer International Publishing: Berlin/Heidelberg, Germany, 2017; pp. 285–292. [CrossRef]
47. Tiersten, H.F. Electromechanical coupling factors and fundamental material constants of thickness vibrating piezoelectric plates. *Ultrasonics* **1970**, *8*, 19–23. [CrossRef]
48. Shi, L.; Liu, N.; Zhou, J.; Zhou, Y.; Wang, J.; Liu, Q. Spectral element method for band-structure calculations of 3D phononic crystals. *J. Phys. Appl. Phys.* **2016**, *49*, 605. [CrossRef]
49. Xu, H.; Cantwell, C.D.; Monteserin, C.; Eskilsson, C.; Engsig-Karup, A.P.; Sherwin, S.J. Spectral/hp element methods: Recent developments, applications, and perspectives. *J. Hydrodyn.* **2018**, *30*, 1–22. [CrossRef]
50. Vatulyan, A.; Baranov, I. Determination of the crack configuration in an anisotropic elastic medium. *Acoust. Phys.* **2005**, *51*, 385–391. [CrossRef]
51. Wang, L.; Yuan, F. Group velocity and characteristic wave curves of Lamb waves in composites: Modeling and experiments. *Compos. Sci. Technol.* **2007**, *67*, 1370–1384. [CrossRef]

Disclaimer/Publisher's Note: The statements, opinions and data contained in all publications are solely those of the individual author(s) and contributor(s) and not of MDPI and/or the editor(s). MDPI and/or the editor(s) disclaim responsibility for any injury to people or property resulting from any ideas, methods, instructions or products referred to in the content.